

Random singlet state in $\text{Ba}_5\text{CuIr}_3\text{O}_{12}$ single crystals

Pavel A. Volkov,^{1,2,*} Choong-Jae Won,^{3,4} D. I. Gorbunov,⁵ Jaewook Kim,^{1,6} Mai Ye,^{1,†}
Heung-Sik Kim,^{1,7} J. H. Pixley,^{1,2} Sang-Wook Cheong,^{1,3,4,6} and G. Blumberg^{1,8,‡}

¹*Department of Physics and Astronomy, Rutgers University, Piscataway, NJ 08854, USA*

²*Center for Materials Theory, Rutgers University, Piscataway, New Jersey, 08854, USA*

³*Max Planck POSTECH/Korea Research Initiative,*

Pohang University of Science and Technology, Pohang 37673, Korea

⁴*Laboratory of Pohang Emergent Materials, Pohang Accelerator Laboratory, Pohang 37673, Korea*

⁵*Hochfeld-Magnetlabor Dresden (HLD-EMFL), Helmholtz-Zentrum Dresden-Rossendorf, 01328 Dresden, Germany*

⁶*Rutgers Center for Emergent Materials, Rutgers University, Piscataway, NJ 08854, USA*

⁷*Department of Physics, Kangwon National University, Chuncheon 24341, Korea*

⁸*National Institute of Chemical Physics and Biophysics, 12618 Tallinn, Estonia*

(Dated: January 20, 2020)

We study the thermodynamic and high-magnetic-field properties of the magnetic insulator $\text{Ba}_5\text{CuIr}_3\text{O}_{12}$, which shows no magnetic order down to 2K consistent with a spin liquid ground state. While the temperature dependence of the magnetic susceptibility and the specific heat shows only weak antiferromagnetic correlations, we find that the magnetization does not saturate up to a field of 59 Tesla, leading to an apparent contradiction. We demonstrate that the paradox can be resolved, and all of the experimental data can be consistently described within the framework of random singlet states. We demonstrate a generic procedure to derive the exchange coupling distribution $P(J)$ from the magnetization measurements and use it to show that the experimental data is consistent with the power-law form $P(J) \sim J^{-\alpha}$ with $\alpha \approx 0.6$. Thus, we reveal that high-magnetic-field measurements can be essential to discern quantum spin liquid candidates from disorder dominated states that do not exhibit long-range order.

Strong quantum fluctuations in insulating magnetic compounds can give rise to quantum spin liquid (QSL) ground states, where the interaction-driven ordering tendencies are thwarted completely. Devoid of long-range order, QSLs lie beyond the Landau symmetry-based classification, and are characterized instead by their unconventional entanglement properties and the presence of exotic fractionalized excitations [1, 2]. However, identifying the elusive QSL behavior in real materials has proven to be a formidable task [2–4]. The search for QSL candidate materials represents a major challenge of modern condensed matter physics.

Disorder is one of the major hindrances to identify QSL materials [5–7], as it can drive the formation of random singlet states (RSS) [8] or disordered stripe states [9] instead of a QSL. Importantly, this includes single-crystal samples due to intrinsic disorder [10, 11]. A convenient reference point can be found in one-dimensional (1D) systems, where the quantum fluctuations are dominant [12] and the effect of disorder was clarified some time ago [13, 14]. In 1D it converts the spin liquid ground state into a RSS, where the effective exchange coupling follows a broad probability distribution that has a universal form [15] at low energies. In 2D and 3D, on the contrary, the fate of disordered spin systems is still an open question. While a random singlet state with a power-law distribution has been conjectured [16], the true ground state of such systems is still under debate and might not be universal [17–19]. In particular, enhanced suppression of QSL states by disorder has been found in model calculations [19, 20]. However, mechanisms for the stabilization

of QSL states by disorder have also been proposed [21]. Additionally, a strong spin-orbit coupling (SOC) is an important ingredient in many QSL candidates. While its effects on clean QSLs have been studied [1, 2] and particularly emphasized for the so-called Kitaev materials [22, 23], the interplay of SOC with disorder still remains to be understood. Thus, careful studies on the role of disorder and SOC in materials showing QSL-like behavior (i.e., no ordering or glassiness down to the lowest temperatures) are of the utmost importance to confirm, or rule out, the QSL state.

In this Rapid Communication, we study the magnetic and thermodynamic properties of the insulating iridate $\text{Ba}_5\text{CuIr}_3\text{O}_{12}$, which features a quasi-1D arrangement of alternating Cu^{2+} ions and Ir^{4+} trimers [25, 26] (see Fig. 1). This iridate is of particular interest for the following reasons. First, previous studies [25] have shown that no magnetic ordering occurs in $\text{Ba}_5\text{CuIr}_3\text{O}_{12}$ down to 4 K despite a Curie temperature of -98 K, which suggests a possible QSL ground state. Moreover, a related compound $\text{Ba}_4\text{NbIr}_3\text{O}_{12}$ has recently been proposed to be a QSL candidate material [27]. Second, the nature of the Ir magnetic moments in this system is quite peculiar. The $5d$ Ir ions have a strong spin-orbit coupling and form face-sharing Ir^{4+} trimers, which renders the usual local $J_{\text{eff}}=1/2$ moment picture [28, 29] inapplicable due to enhanced covalency. Instead, molecular orbitals at each Ir trimer are expected to form [24, 27, 30]. Finally, the material contains intrinsic disorder due to site mixing between Cu and Ir, as well as Cu displacement from the prism center [25, 26] [see Fig. 1 (a)]. The former can

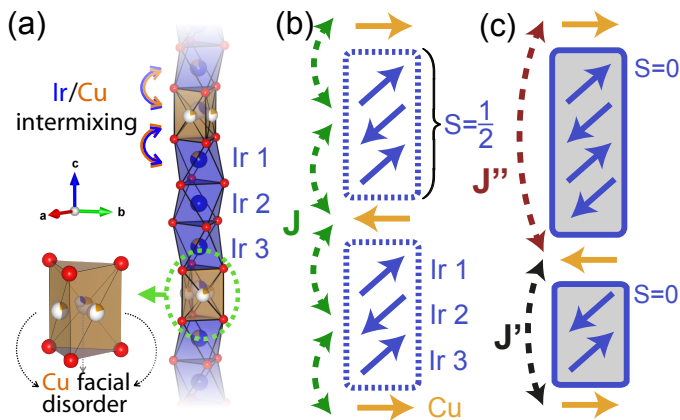


FIG. 1. The depiction of intrinsic disorder in chains of Cu and Ir in the $\text{Ba}_5\text{CuIr}_3\text{O}_{12}$ lattice structure. (a) Cu-Ir chains composed of Ir^{4+} trimers and Cu^{2+} ions (Ba ions fill the space between the chains [24]). Disorder occurs either due to Cu-Ir site mixing or due to Cu being displaced from the prism center [25, 26]. (b) Spin degrees of freedom in a chain segment, here Ir trimers form effective $J = 1/2$ moments that interact with the Cu^{2+} spins. (c) An example of disorder in the position of Cu and Ir leading to exchange disorder. Interchanging the Cu and Ir sites leads to Ir clusters forming low-spin states. The Cu spins interact with each other through perturbatively generated J' and J'' resulting in disorder in the effective magnetic exchange couplings.

lead to randomness (i.e. disorder) in the exchange couplings. A particular scenario is shown in Fig. 1 (c), where interchanging Cu and Ir within a unit cell transforms two Ir trimers into a dimer and tetramer with a possible $S = 0$ ground state. As a result, the remaining Cu spins interact by means of perturbatively generated exchange couplings, that are different from the initial non-random value. All of the above makes $\text{Ba}_5\text{CuIr}_3\text{O}_{12}$ a well-suited candidate to explore the interplay of QSL physics with intrinsic disorder and strong spin-orbit coupling.

We have performed magnetic susceptibility, specific heat, and high-field magnetization measurements. We demonstrate that these data combined point unambiguously to $\text{Ba}_5\text{CuIr}_3\text{O}_{12}$ being in a random singlet state with a power-law distribution of exchange couplings, and thus ruling out QSL behavior. As such, we show how the high field magnetization measurements are essential to reveal and characterize a RSS in materials that otherwise show QSL-like behavior.

Experimental techniques. We have grown single crystals of $\text{Ba}_5\text{CuIr}_3\text{O}_{12}$ using the flux method. The crystal structure and orientation were confirmed by x-ray diffraction and Laue measurements [31]. The magnetic susceptibility was measured using a superconducting quantum interference device (SQUID) magnetometer (Quantum Design) in an applied field of 0.1 T on warming after zero-field cooling to 1.8 K. The specific heat of $\text{Ba}_5\text{CuIr}_3\text{O}_{12}$ single crystals was measured using a Physical Property Measurement System (Quantum Design

Dynacool). The high-field magnetization measurements have been performed at 2 K in pulsed magnetic fields up to 59 T [31] using the facilities at the Dresden High Field Magnetic Field Laboratory, described in Refs. [32–34].

Magnetic susceptibility. In Fig. 2(a) we show the temperature dependence of the magnetic susceptibility for fields along the c axis $\chi^c(T)$ or in the $a-b$ plane $\chi^{ab}(T)$. Both $\chi^c(T)$ and $\chi^{ab}(T)$ show a featureless monotonic increase towards low temperatures and a weak anisotropy [31]. At high temperatures, a constant contribution χ_0 in addition to the Curie behavior can be identified, which is attributed to Van Vleck paramagnetism. The effective moment that is obtained from the Curie law fit is $\mu_{\text{eff}} = 2.2\mu_B$, which is close to the value that is expected from one Cu^{2+} moment ($\mu_{\text{eff}}^{\text{Cu}} = 1.9\mu_B$) and one Ir trimer ($\mu_{\text{eff}}^{\text{Ir-tr}} = 0.8\mu_B$) [27] that yield $\sqrt{(\mu_{\text{eff}}^{\text{Cu}})^2 + (\mu_{\text{eff}}^{\text{Ir-tr}})^2} \approx 2.06\mu_B$.

In an earlier study on polycrystalline samples [25], the susceptibility was analyzed using a modified Curie-Weiss model for temperatures between 150 K and 300 K. Using $\chi(T) = C/(T - T_W) + \chi_0$ resulted in a large negative Weiss temperature $T_W = -98$ K. Analyzing our data, we have come to the conclusion that the Curie-Weiss model does not provide an adequate description. First, if the analysis is restricted to high temperatures, large uncertainties in the value of T_W result [31]. Second, at low temperatures $(\chi - \chi_0)^{-1}$ is not linear as would have been expected from the Curie-Weiss form. We demonstrate this in the inset of Fig. 2 (a) by showing $(T - T_W)(\chi^c - \chi_0^c)^{-1}$ for a range of T_W from -3 K to -5 K. Additionally, one can see that larger or smaller values of T_W would lead to even larger deviations, suggesting weak antiferromagnetic (AFM) correlations.

This is further corroborated by noting that even in the absence of order, anomalies in $\chi(T)$ are expected to arise at a temperature corresponding to the interaction scale in 1D antiferromagnetic chains [35, 36], spin glasses [37, 38], and spin liquids with AFM interactions [39]. The absence of such features in Fig. 2 (a) implies that the relevant interaction scale is lower than 2 K. We have also confirmed the absence of glassy behavior above 2 K by performing low-field (100 Oe) field-cooled/zero-field-cooled (FC/ZFC) susceptibility measurements [31].

Specific heat. In Fig. 2(b) we show the temperature dependence of the specific heat $C_P(T)$. The high-temperature behavior of $C_P(T)/T$ is dominated by the phonon contribution, which freezes out as the temperature is lowered. Thus, the dramatic upturn that is observed below ~ 10 K must be of magnetic origin. As no Schottky-like peak is observed down to 2 K, the energy scale associated with these magnetic excitations should be below 2 K. This is consistent with the weak AFM correlations conjectured above on the basis of the $\chi(T)$ measurements.

High-field magnetization. Surprisingly, the field depen-

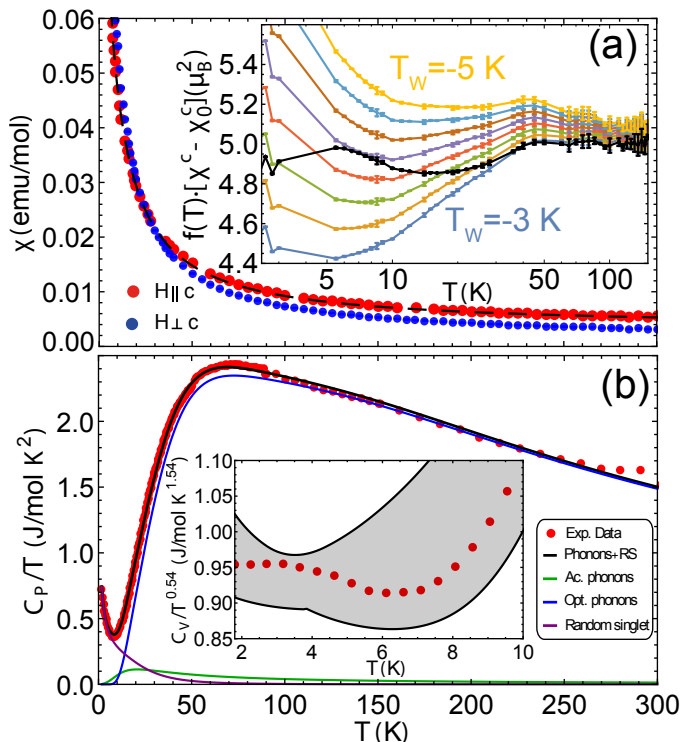


FIG. 2. Temperature (T) dependencies of the magnetic susceptibility (χ) and the specific heat (C_P). (a) The magnetic susceptibility, data in red ($H \parallel c$) and blue ($H \perp c$). The black dashed line is a fit for $H \parallel c$ with the random singlet model $\chi_{RS} = \partial M_{RS} / \partial H$, see Eq. (1). Inset: $(\chi^c - \chi_0^c)$ multiplied by a function $f(T)$. For the colored points we take $f(T) = 3(T - T_W)$ for several values of T_W between -3 K and -5 K, for $H \parallel c$ demonstrating the nonlinearity of the low temperature dependence. Black points are the RSS contribution $f(T) = \chi_{RS}(T) / \mu_{eff}^2$. Lines are guide to the eye. At high temperatures all curves converge to μ_{eff}^2 . (b) Specific heat divided by temperature. The black line is a fit to the combination of the random singlet model in Eq. (2) and a simplified model for phonons (see text). Inset: The specific heat divided by $T^{0.54}$; the gray band shows the confidence interval of the fit.

dence of the magnetization $M(H)$ is in stark contrast with the expectation from weak AFM correlations, see Fig. 3. Namely, $M(H)$ shows a monotonic increase without saturation up to the highest fields measured, 59 T. To illustrate this, we show in Fig. 3 (green line) the $M(H)$ that is expected for a system of two free $S = 1/2$ spins per unit cell, with an effective moment $\mu_{eff} / \sqrt{2}$ each, and taking the Van Vleck contribution $M_{VV} = \chi_0 H$ into account. One can see that within such a model the magnetization would have saturated well below 59 T, implying that the magnetic interactions in $\text{Ba}_5\text{CuIr}_3\text{O}_{12}$ must be rather strong. One can estimate the scale of the interactions assuming the $S = 1/2$ moments mentioned above to form singlets with an isotropic exchange energy J . The magnetization would then saturate when the Zeeman en-

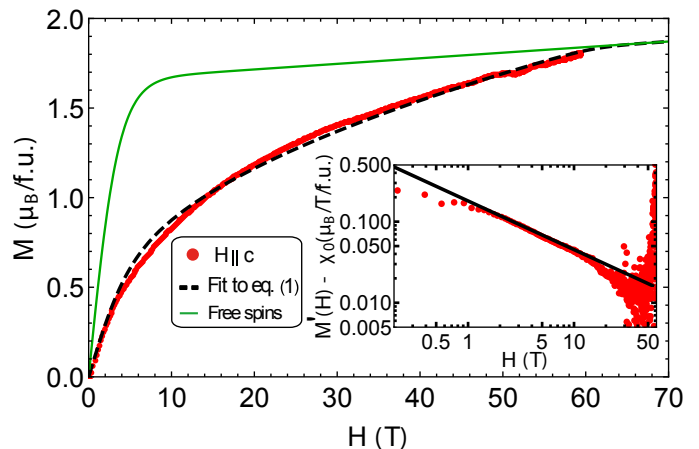


FIG. 3. The magnetic field dependence of the magnetization at $T = 2$ K for the field along the c -axis direction. The weak kink near 50 T results from the noise of the equipment. The black dashed line is a fit with the random singlet model, Eq. (1), using the parameters given in Table S2. The green line represents the magnetization of an $S = 1/2$ paramagnet. The Van Vleck contribution $H\chi_0$ has been added to both. Inset: Log-Log plot of $dM(H)/dH - \chi_0$ for the field along the c -axis, and the black line is a power-law fit $0.18H^{-0.6}$. Data for $H \parallel ab$ are not shown due to calibration issues [31].

ergy $E_Z = HgS = H\mu_{eff}\sqrt{S/(S+1)}$ for the triplet excitation reaches J , see Fig. 4. As the saturation field is at least larger than 59 T, we estimate $J \gtrsim 70$ K. On the contrary, the energy scales we have derived above from the susceptibility and specific heat measurements are below 2 K. In addition, in systems with AFM interactions the shape of the magnetization curve as a function of H is usually convex [35, 40–42] at low temperatures, while the $M(H)$ curve shown in Fig. 3 is clearly concave, further making the interpretation of the high-field magnetization in terms of a strong AFM exchange interaction problematic.

Random singlet state. We will now show that the conflict between the energy scales that we have seen in low- and high-field measurements can be resolved by assuming a *distribution* of energy scales in the system in the framework of a RSS. The exchange disorder driving the RSS can result from the intrinsic positional disorder between Cu and Ir observed in x-ray [25] and neutron scattering [26] experiments, as discussed above and illustrated for a particular scenario in Fig. 1 (c). Other possible scenarios would involve nonstoichiometric compositions within one unit cell, e.g., simply substituting one Cu for Ir.

Given the small magnetic anisotropy observed in $\chi(T)$ [see Fig. 2 (a)], we consider an ensemble of singlets formed by two effective $S = 1/2$ moments with a total magnetic moment μ , and with an isotropic random exchange coupling J that is drawn from the distribution $P(J)$. The magnetization of the whole system is then an average of the magnetization of each isolated singlet, and

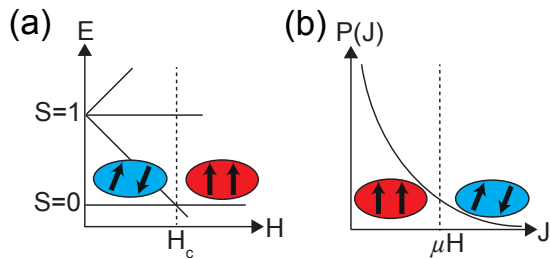


FIG. 4. (a) The energy levels and the ground state of an isolated singlet. The triplet ($S = 1$) of excited states at $H = 0$ is split in the field, and a change of the ground state occurs at $H_c(J)$, from singlet ($S = 0$) to fully polarized ($S = 1$). (b) The random singlet distribution in a magnetic field. Singlets with $J < \mu H$ are broken by the field and are fully polarized, while the ones with $J > \mu H$ remain in the singlet state, leading to a non-saturating magnetization.

is given by

$$M_{RS}(H) = \int_0^\infty dJ P(J) \frac{2\mu \sinh(\beta\mu H)}{2 \cosh(\beta\mu H) + 1 + e^{\beta J}}, \quad (1)$$

where $\beta = 1/(k_B T)$. We account for the Van Vleck contribution as before for free spins, i.e., $M(H) = M_{RS}(H) + H\chi_0$. Qualitatively, Eq. (1) allows a coexistence of almost free spins that can yield a diverging susceptibility towards $T = 0$ and strongly bound singlets from the high- J tail of the distribution that require the applied field to be above a threshold value for the magnetization to saturate (see Fig. 4). Importantly, in the limit $T \ll \mu H$ one obtains from Eq. (1) that $M'(H) \approx \chi_0 + \mu^2 P(\mu H)$, allowing one to extract the functional form of the distribution $P(J)$ directly from the experimental data. We find that $P(\mu H)$ follows the power-law form $P(\mu H) \sim H^{-0.6}$ for fields between 1 and 15 T (see Fig. 3, inset).

Let us now discuss the specific heat. Similarly to the magnetization, the contribution of the RSS is an average over specific heats of individual singlets

$$C_{RS}(T) = k_B \int_0^\infty dJ P(J) \frac{J^2}{T^2} \frac{3e^{-J/T}}{(1 + 3e^{-J/T})^2}. \quad (2)$$

For $P(J) \sim J^{-\alpha}$ it follows that at low temperatures $C_{RS} \sim T^{(1-\alpha)}$. Indeed, we find that below about 4 K, $C_P \sim T^{0.54}$ [see Fig. 2 (b), inset], that suggests the power-law exponent to be 0.46. The discrepancy of this value with the one obtained from the high-field magnetization can be attributed to $P(J)$ having a slightly different form for low and moderate J , as the specific heat (2) is most sensitive to $P(J)$ below $J \approx 4$ K, while the power-law in the magnetization is extracted for larger values of J . Nonetheless, the discrepancy between the power-law exponents is not too large.

Hence, we have attempted to fit the data from each measurement with a single form of $P(J) = \theta(J_0 - J)J^{-\alpha}$, where a cutoff scale J_0 has been introduced to ensure

TABLE I. The power-law exponents α and the cutoff scale J_0 are obtained by fitting the magnetic susceptibility, magnetization, and heat capacity data with the corresponding confidence intervals. The resulting fits are plotted in Figs. 2 and 3.

Measured Quantity	α	J_0 (K)
$\chi^c(T)$	0.62 ± 0.02	36 ± 1
$\chi^{ab}(T)$	0.66 ± 0.01	16.3 ± 0.4
$M_c(H)$	0.64 ± 0.01	67.8 ± 0.4
$C_p(T)$	0.55 ± 0.05	95 ± 5

proper normalization. The results of the fits are given in Table S2. The parameter μ in Eq. (1) is related to μ_{eff} at high temperatures as $\mu = \sqrt{2/3} \mu_{\text{eff}}$. Additionally, to describe the specific heat at all temperatures, we have modeled the phonon contribution of specific heat with a combination of Debye and Einstein phonons [31], i.e. $C_P(T) = C_{RS}(T) + C_{\text{phon}}(T)$.

The resulting fits to the data are excellent as shown in Figs. 2 and 3. Importantly, the qualitative features of all three measurements are well captured: the susceptibility increasing nonlinearly at low- T [see the inset of Fig. 2 (a)], the upturn in the specific heat at low- T where C_{RS} dominates, and the non-saturating concave high-field magnetization. Moreover, the resulting power-law exponents obtained from fits across different experiments agree well with each other (see Table S2). The cutoff scale J_0 , on the contrary, shows significant variations. This can be partially attributed to the deviations of $P(J)$ from the power-law form at the lowest and highest values of J (as is seen in Fig. 3), as different quantities are most sensitive to different ranges of J values. Additionally, it can be shown that this parameter depends on the way the cutoff is implemented - e.g., implementation of a soft cutoff affects the value of J_0 [31]. Thus, we argue that the variations of J_0 reflect the approximate character of the form of $P(J)$ we use, which is nonetheless sufficient for the qualitative description of the data.

As has been mentioned above, the distribution parameters may vary between the low and intermediate energy scales. The agreement of the power-law exponents in Table S2 with the one obtained from magnetization between 1 and 15 T suggests that these values do not concern the distribution at very low energies. Instead, we have established the presence of random singlet excitations with a unique power-law form in the intermediate energy range.

Summary. By combining low- and high- magnetic field measurements we have established that $\text{Ba}_5\text{CuIr}_3\text{O}_{12}$ at low temperatures is well described as a random singlet state. We have shown that a non-saturating high-field magnetization allows one to rule out a QSL scenario and quantitatively extract the exchange coupling distribution of the random singlet state $P(J) \sim J^{-0.6}$ at intermediate energies. We find the extracted power-law distribution is consistent across the magnetization, susceptibility, and

specific heat measurements. Thus, we establish that a combination of high-field measurements with more conventional techniques allows one to study the role of disorder in QSL candidate materials as well as characterize strongly disordered ground states.

Acknowledgments. Crystal growth was supported by the National Research Foundation of Korea, Ministry of Science and ICT (No. 2016K1A4A4A01922028), and magnetic measurement was supported by the NSF under Grant No. DMR-1629059. We acknowledge the support of HLD at HZDR, member of the European Magnetic Field Laboratory (EMFL). The work was supported by the DFG through SFB 1143. The spectroscopic characterization at Rutgers (M.Y. and G.B.) was supported by NSF Grant No. DMR-1709161. J. H. P. was supported by Grant No. 2018058 from the United States-Israel Binational Science Foundation (BSF), Jerusalem, Israel and acknowledges the Aspen Center for Physics where some of this work was performed, which is supported by National Science Foundation Grant No. PHY-1607611. P.A.V. acknowledges the support by the Rutgers University Center for Materials Theory Postdoctoral fellowship.

* pv184@physics.rutgers.edu

† mye@physics.rutgers.edu

‡ girsh@physics.rutgers.edu

- [1] Lucile Savary and Leon Balents, “Quantum spin liquids: a review,” *Reports on Progress in Physics* **80**, 016502 (2016).
- [2] Yi Zhou, Kazushi Kanoda, and Tai-Kai Ng, “Quantum spin liquid states,” *Rev. Mod. Phys.* **89**, 025003 (2017).
- [3] M. R. Norman, “Colloquium: Herbertsmithite and the search for the quantum spin liquid,” *Rev. Mod. Phys.* **88**, 041002 (2016).
- [4] Jinsheng Wen, Shun-Li Yu, Shiyan Li, Weiqiang Yu, and Jian-Xin Li, “Experimental identification of quantum spin liquids,” *npj Quantum Materials* **4**, 12 (2019).
- [5] J. S. Helton, K. Matan, M. P. Shores, E. A. Nytko, B. M. Bartlett, Y. Qiu, D. G. Nocera, and Y. S. Lee, “Dynamic scaling in the susceptibility of the spin- $\frac{1}{2}$ kagome lattice antiferromagnet herbertsmithite,” *Phys. Rev. Lett.* **104**, 147201 (2010).
- [6] Itamar Kimchi, John P. Sheckelton, Tyrel M. McQueen, and Patrick A. Lee, “Scaling and data collapse from local moments in frustrated disordered quantum spin systems,” *Nature Communications* **9** (2018), 10.1038/s41467-018-06800-2.
- [7] Y. S. Choi, C. H. Lee, S. Lee, Sungwon Yoon, W.-J. Lee, J. Park, Anzar Ali, Yogesh Singh, Jean-Christophe Orain, Gareoung Kim, Jong-Soo Rhyee, Wei-Tin Chen, Fangcheng Chou, and Kwang-Yong Choi, “Exotic Low-Energy Excitations Emergent in the Random Kitaev Magnet Cu_2IrO_3 ,” *Phys. Rev. Lett.* **122**, 167202 (2019).
- [8] Itamar Kimchi, Adam Nahum, and T. Senthil, “Valence Bonds in Random Quantum Magnets: Theory and Application to YbMgGaO_4 ,” *Phys. Rev. X* **8**, 031028 (2018).
- [9] Zhenyue Zhu, P. A. Maksimov, Steven R. White, and A. L. Chernyshev, “Disorder-Induced Mimicry of a Spin Liquid in YbMgGaO_4 ,” *Phys. Rev. Lett.* **119**, 157201 (2017).
- [10] Yuesheng Li, Gang Chen, Wei Tong, Li Pi, Juanjuan Liu, Zhaorong Yang, Xiaoqun Wang, and Qingming Zhang, “Rare-Earth Triangular Lattice Spin Liquid: A Single-Crystal Study of YbMgGaO_4 ,” *Phys. Rev. Lett.* **115**, 167203 (2015).
- [11] Yuesheng Li, Sebastian Bachus, Benqiong Liu, Igor Radelytskyi, Alexandre Bertin, Astrid Schneidewind, Yoshifumi Tokiwa, Alexander A. Tsirlin, and Philipp Gegenwart, “Rearrangement of Uncorrelated Valence Bonds Evidenced by Low-Energy Spin Excitations in YbMgGaO_4 ,” *Phys. Rev. Lett.* **122**, 137201 (2019).
- [12] T. Giamarchi, *Quantum Physics in One Dimension* (Oxford University Press, New York, 2004).
- [13] Shang-keng Ma, Chandan Dasgupta, and Chin-kun Hu, “Random antiferromagnetic chain,” *Phys. Rev. Lett.* **43**, 1434–1437 (1979).
- [14] Jorge E. Hirsch and Jorge V. José, “Singular thermodynamic properties in random magnetic chains,” *Phys. Rev. B* **22**, 5339–5354 (1980).
- [15] Daniel S. Fisher, “Random antiferromagnetic quantum spin chains,” *Phys. Rev. B* **50**, 3799–3821 (1994).
- [16] R. N. Bhatt and P. A. Lee, “Scaling studies of highly disordered spin-1/2 antiferromagnetic systems,” *Phys. Rev. Lett.* **48**, 344–347 (1982).
- [17] Olexei Motrunich, Siun-Chuon Mau, David A. Huse, and Daniel S. Fisher, “Infinite-randomness quantum ising critical fixed points,” *Phys. Rev. B* **61**, 1160–1172 (2000).
- [18] Y.-C. Lin, R. Mélin, H. Rieger, and F. Igloi, “Low-energy fixed points of random heisenberg models,” *Phys. Rev. B* **68**, 024424 (2003).
- [19] Hikaru Kawamura, Ken Watanabe, and Tokuro Shimokawa, “Quantum spin-liquid behavior in the spin-1/2 random-bond heisenberg antiferromagnet on the kagome lattice,” *Journal of the Physical Society of Japan* **83**, 103704 (2014), <https://doi.org/10.7566/JPSJ.83.103704>.
- [20] Kazuki Uematsu and Hikaru Kawamura, “Randomness-induced quantum spin liquid behavior in the $s = \frac{1}{2}$ random $J_1 - J_2$ heisenberg antiferromagnet on the square lattice,” *Phys. Rev. B* **98**, 134427 (2018).
- [21] Han-Qing Wu, Shou-Shu Gong, and D. N. Sheng, “Randomness-induced spin-liquid-like phase in the spin- $\frac{1}{2}$ $J_1 - J_2$ triangular heisenberg model,” *Phys. Rev. B* **99**, 085141 (2019).
- [22] J. Knolle and R. Moessner, “A field guide to spin liquids,” *Annual Review of Condensed Matter Physics* **10**, 451–472 (2019), <https://doi.org/10.1146/annurev-conmatphys-031218-013401>.
- [23] Hidenori Takagi, Tomohiro Takayama, George Jackeli, Giniyat Khaliullin, and Stephen E. Nagler, “Kitaev quantum spin liquid - concept and materialization,” [arXiv:1903.08081](https://arxiv.org/abs/1903.08081).
- [24] Mai Ye, Heung-Sik Kim, Jae-Wook Kim, Choong-Jae Won, Kristjan Haule, David Vanderbilt, Sang-Wook Cheong, and G. Blumberg, “Covalency-driven collapse of strong spin-orbit coupling in face-sharing iridium octahedra,” *Phys. Rev. B* **98**, 201105 (2018).
- [25] Graeme R. Blake, Jeremy Sloan, Jaap F. Vente, and Peter D. Battle, “Prediction and Verification of the Structural Chemistry of New One-Dimensional Bar-

- ium/Copper/Iridium Oxides,” *Chem. Mat.* **10**, 3536–3547 (1998).
- [26] Graeme R. Blake, Peter D. Battle, Jeremy Sloan, Jaap F. Vente, Jacques Darriet, and François Weill, “Neutron Diffraction Study of the Structures of $\text{Ba}_5\text{CuIr}_3\text{O}_{12}$ and $\text{Ba}_{16}\text{Cu}_3\text{Ir}_{10}\text{O}_{39}$,” *Chem. Mat.* **11**, 1551–1558 (1999).
- [27] Loi T. Nguyen and R. J. Cava, “Trimer-based spin liquid candidate $\text{Ba}_4\text{NbIr}_3\text{O}_{12}$,” *Phys. Rev. Materials* **3**, 014412 (2019).
- [28] B. J. Kim, Hosub Jin, S. J. Moon, J.-Y. Kim, B.-G. Park, C. S. Leem, Jaejun Yu, T. W. Noh, C. Kim, S.-J. Oh, J.-H. Park, V. Durairaj, G. Cao, and E. Rotenberg, “Novel $J_{\text{eff}} = 1/2$ Mott State Induced by Relativistic Spin-Orbit Coupling in Sr_2IrO_4 ,” *Phys. Rev. Lett.* **101**, 076402 (2008).
- [29] B. J. Kim, H. Ohsumi, T. Komesu, S. Sakai, T. Morita, H. Takagi, and T. Arima, “Phase-Sensitive Observation of a Spin-Orbital Mott State in Sr_2IrO_4 ,” *Science* **323**, 1329–1332 (2009).
- [30] S V Streltsov and D I Khomskii, “Orbital physics in transition metal compounds: new trends,” *Physics-Uspekhi* **60**, 1121–1146 (2017).
- [31] See Supplemental Material below for the details of crystal growth procedure, calibration of the high-field measurements, random singlet model and the fitting procedure as well as magnetic anisotropy and zero-field cooled measurements, which includes Refs. [24–27, 43–47].
- [32] S. Zherlitsyn, A. D. Bianchi, T. Herrmannsdoerfer, F. Pobell, Y. Skourski, A. Sytcheva, S. Zvyagin, and J. Wosnitzer, “Coil design for non-destructive pulsed-field magnets targeting 100 t,” *IEEE Transactions on Applied Superconductivity* **16**, 1660–1663 (2006).
- [33] J. Wosnitzer, A.D. Bianchi, J. Freudenberger, J. Haase, T. Herrmannsdorfer, N. Kozlova, L. Schultz, Y. Skourski, S. Zherlitsyn, and S.A. Zvyagin, “Dresden pulsed magnetic field facility,” *Journal of Magnetism and Magnetic Materials* **310**, 2728 – 2730 (2007), proceedings of the 17th International Conference on Magnetism.
- [34] Y. Skourski, M. D. Kuz’min, K. P. Skokov, A. V. Andreev, and J. Wosnitzer, “High-field magnetization of $\text{ho}_2\text{fe}_{17}$,” *Phys. Rev. B* **83**, 214420 (2011).
- [35] Jill C. Bonner and Michael E. Fisher, “Linear Magnetic Chains with Anisotropic Coupling,” *Phys. Rev.* **135**, A640–A658 (1964).
- [36] Sebastian Eggert, Ian Affleck, and Minoru Takahashi, “Susceptibility of the spin 1/2 heisenberg antiferromagnetic chain,” *Phys. Rev. Lett.* **73**, 332–335 (1994).
- [37] K. Binder and A. P. Young, “Spin glasses: Experimental facts, theoretical concepts, and open questions,” *Rev. Mod. Phys.* **58**, 801–976 (1986).
- [38] J A Mydosh, “Spin glasses: redux: an updated experimental/materials survey,” *Reports on Progress in Physics* **78**, 052501 (2015).
- [39] Junki Yoshitake, Joji Nasu, and Yukitoshi Motome, “Fractional spin fluctuations as a precursor of quantum spin liquids: Majorana dynamical mean-field study for the kitaev model,” *Phys. Rev. Lett.* **117**, 157203 (2016).
- [40] Robert B. Griffiths, “Magnetization curve at zero temperature for the antiferromagnetic heisenberg linear chain,” *Phys. Rev.* **133**, A768–A775 (1964).
- [41] V. A. Kashurnikov, N. V. Prokof’ev, B. V. Svistunov, and M. Troyer, “Quantum spin chains in a magnetic field,” *Phys. Rev. B* **59**, 1162–1167 (1999).
- [42] Tokuro Shimokawa, Ken Watanabe, and Hikaru Kawamura, “Static and dynamical spin correlations of the $s = \frac{1}{2}$ random-bond antiferromagnetic heisenberg model on the triangular and kagome lattices,” *Phys. Rev. B* **92**, 134407 (2015).
- [43] Giniyat Khaliullin, “Orbital Order and Fluctuations in Mott Insulators,” *Progress of Theoretical Physics Supplement* **160**, 155–202 (2005), <http://oup.prod.sis.lan/ptps/article-pdf/doi/10.1143/PTPS.160.155/5162453/160-155.pdf>.
- [44] Jeffrey G. Rau, Eric Kin-Ho Lee, and Hae-Young Kee, “Spin-orbit physics giving rise to novel phases in correlated systems: Iridates and related materials,” *Annual Review of Condensed Matter Physics* **7**, 195–221 (2016), <https://doi.org/10.1146/annurev-conmatphys-031115-011319>.
- [45] Joel Bertinshaw, Y.K. Kim, Giniyat Khaliullin, and B.J. Kim, “Square lattice iridates,” *Annual Review of Condensed Matter Physics* **10**, 315–336 (2019), <https://doi.org/10.1146/annurev-conmatphys-031218-013113>.
- [46] K. A. Modic, Tess E. Smidt, Itamar Kimchi, Nicholas P. Breznay, Alun Biffin, Sungkyun Choi, Roger D. Johnson, Radu Coldea, Pilanda Watkins-Curry, Gregory T. McCandless, Julia Y. Chan, Felipe Gandara, Z. Islam, Ashvin Vishwanath, Arkady Shekhter, Ross D. McDonald, and James G. Analytis, “Realization of a three-dimensional spin-anisotropic harmonic honeycomb iridate,” *Nature Communications* **5**, 4203 (2014).
- [47] Hiroaki Ishizuka, “Temperature-dependent magnetic anisotropy from pseudo-dipolar interactions,” *Phys. Rev. B* **95**, 184413 (2017).

Supplemental Material for: Random singlet state in $\text{Ba}_5\text{CuIr}_3\text{O}_{12}$ single crystals

Single Crystal Growth

For the $\text{Ba}_5\text{CuIr}_3\text{O}_{12}$ single crystal growth, we first prepared polycrystalline material by the solid-state reaction method: a stoichiometric composition of BaCO_3 , IrO_2 and CuO powders (Alfa Aeser) were grounded, and the pelletized powder was sintered in the air at 1000 – 1200 C with intermediate grindings. Then $\text{Ba}_5\text{CuIr}_3\text{O}_{12}$ single crystals were grown by flux method using K_2CO_3 with added BaCO_3 . The $\text{Ba}_5\text{CuIr}_3\text{O}_{12}$ polycrystalline powder were mixed with the flux of K_2CO_3 and BaCO_3 , and then were melted in alumina crucible at 1050 °C and slowly cooled down to room temperature at a cooling rate 2 °C/hr. The crystals were washed with hot water to separate from the flux.

XRD measurements of crushed single-crystal powder confirm the right phase (see Fig. S1); the resulting lattice parameters are $a=10.1361\text{\AA}$, $c=21.3561\text{\AA}$. While a agrees to within 0.1% with the previous measurements [25, 26] c is shorter by about 1.4% than the previous reported values [25, 26]. We attribute this discrepancy as well as imperfect match to the predicted intensities to the possible strains and imperfections emerging during crushing. Additionally, we have performed Laue diffraction measurements; the resulting pattern for (001) direction is presented in Fig. S1, right panel. It confirms the single-crystal character of our samples and the threefold pattern symmetry is consistent with the $P3c1$ space group of $\text{Ba}_5\text{CuIr}_3\text{O}_{12}$.

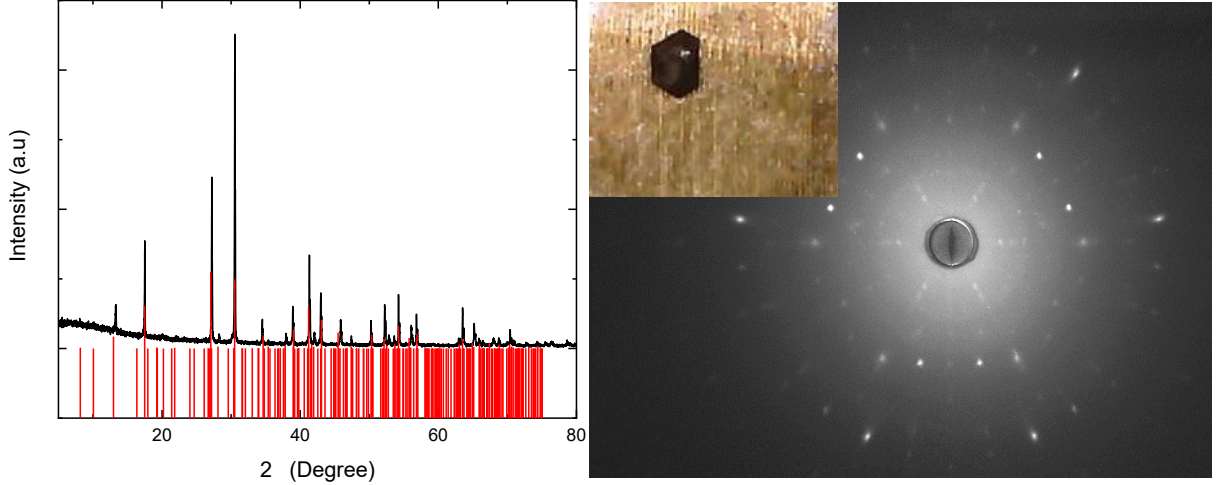


FIG. S1. Left panel: XRD measurement data (black) and intensity pattern expected form $\text{Ba}_5\text{CuIr}_3\text{O}_{12}$ (red lines). Right panel: Laue diffraction data confirming the threefold symmetry and single-crystal nature of the sample. Inset: image of one of the samples on the Laue holder.

Model of the random singlet state

The partition function of a singlet with antiferromagnetic (AFM) interaction J in magnetic field H is (with the singlet state energy set to zero)

$$Z_s = 1 + e^{-\beta J} [2 \cosh(\beta \mu H) + 1]. \quad (\text{S1})$$

And the corresponding magnetization is

$$M_s = -\frac{\partial F}{\partial H} = \mu \frac{2 \sinh(\beta \mu H)}{2 \cosh(\beta \mu H) + 1 + e^{\beta J}}. \quad (\text{S2})$$

The magnetization of the whole system is an average of M_s over a distribution $P(J)$:

$$M = \int_0^\infty dJ P(J) M_s = \int_0^\infty dJ P(J) \mu \frac{2 \sinh(\beta \mu H)}{2 \cosh(\beta \mu H) + 1 + e^{\beta J}}. \quad (\text{S3})$$

On the one hand, if $T \ll \mu H \& J$, M_s is equal to μ for $\mu H > J$ and to 0 otherwise. In this limit, Eq.(S3) simplifies to

$$M = \mu \int_0^{\mu H} dJ P(J) + O[TP(\mu H)]. \quad (\text{S4})$$

The derivative of M with respect to H is then

$$M'(H) = \mu^2 P(\mu H). \quad (\text{S5})$$

On the other hand, if $T \gg \mu H \& J_0$, we have

$$M = \int_0^\infty dJ P(J) \mu \frac{2\beta\mu H}{4} = \frac{\mu^2 H}{2T}, \quad (\text{S6})$$

and

$$M'(H) = \frac{\mu^2}{2T}. \quad (\text{S7})$$

Eq.(S7) is simply the Curie susceptibility $\frac{(g\mu_B)^2 S(S+1)}{3T}$ of two $S=1/2$ spins with g -factor μ/μ_B . We can also calculate the zero-field specific heat from Eq.(S1):

$$C_{RS} = -T k_B \frac{\partial^2 F}{\partial T^2} = \int_0^\infty dJ P(J) \frac{J^2}{T^2} \frac{3e^{-J/T}}{(1+3e^{-J/T})^2}. \quad (\text{S8})$$

Using Eq.(S5) one can extract the distribution $P(J)$ from the low-temperature field dependence of magnetization. Using (S7) the value of the moment μ can be extracted from the high-temperature susceptibility value.

Magnetic anisotropy

In the main text we have concentrated on the data for $H \parallel c$ and generally disregarded the magnetic anisotropy. While it is indeed weak, we provide here additional information regarding this anisotropy and its dependence on the applied field and temperature. In Fig. S2 we show the anisotropy of (a) magnetic susceptibility (b) magnetization, as a function of temperature and magnetic field, respectively. Note that the van Vleck contribution, subtracted from the data in the figure, is also anisotropic: $\chi_0^c = 0.0033$ emu/mol and $\chi_0^{ab} = 0.0012$ emu/mol. To account for the discrepancies in the temperature/field values of the two measurements we use the numerically interpolated values. At large fields or temperatures the anisotropy is seen to decrease. This can be attributed to the anisotropic exchange interactions, characteristic of systems with strong spin-orbit coupling [43] and Ir-based ones in particular [44, 45]. Indeed, temperature-dependent anisotropy has been observed in Ir-based systems [46] and is expected theoretically [47].

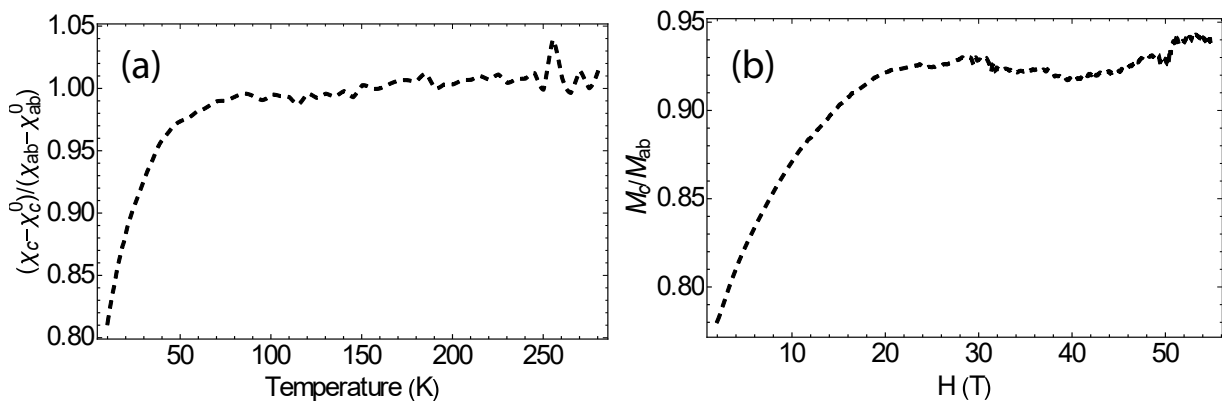


FIG. S2. Anisotropy of (a) magnetic susceptibility (b) magnetization, as a function of temperature and magnetic field, respectively.

FC/ZFC measurements and glassiness

To confirm the absence of glassy behavior in $\text{Ba}_5\text{CuIr}_3\text{O}_{12}$ we have performed ZFC/FC magnetic susceptibility measurements in field of 100 Oe using a SQUID magnetometer (Quantum Design), with the results presented in Fig. S3. We find no signatures of spin freezing or history dependence. The relative differences between the FC and ZFC data are below 2% for both field orientations (for points measured at the same temperature) and can be attributed to the equipment noise (especially taking into account the relatively large background signal, which has been observed to be roughly 10 times larger at this field value than that of an optimally working SQUID).

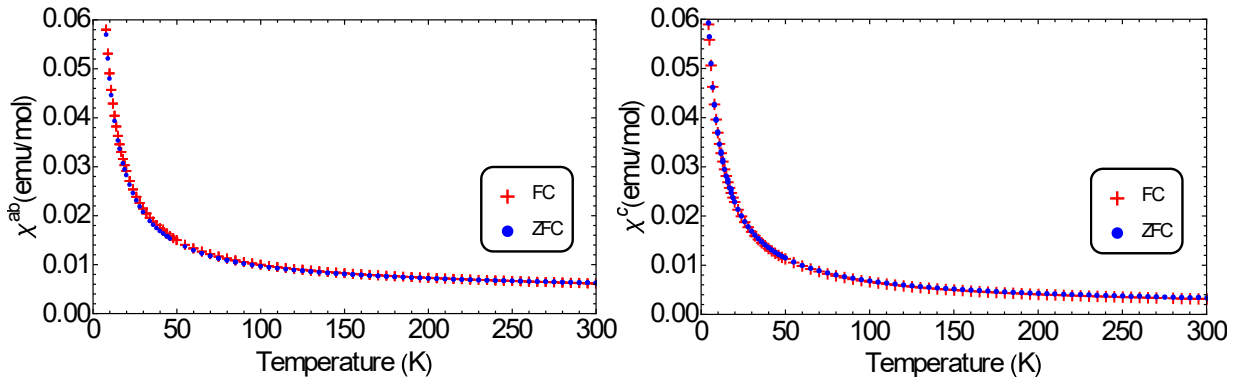


FIG. S3. Comparison of FC and ZFC susceptibility data.

Details of fitting the data

General remarks and choice of random coupling distribution

In main text we have used distribution $P(J) = \theta(J_0 - J)J^{-\alpha}$ for the exchange interaction in the random singlet state, motivated by the magnetization data in Fig. 3, inset. The $\theta(J_0 - J)$ factor is necessary as the integral over the distribution otherwise diverges at large J . While this allows us to satisfactorily describe the data qualitatively, this distribution form is only approximate and thus the values of the parameters extracted from the fits can be model-dependent. Here we show that using a different different way to implement the cutoff may strongly affect the value of J_0 , but not α . Namely, we attempt to fit the experimental data with the distribution $P(J, \sigma) = \frac{J^{-\alpha}}{e^{(J-J_0)/\sigma} + 1}$, where $\sigma \rightarrow 0$ results in the distribution used in the main text. The results of the fits for several values of σ are given in Table S1. Indeed, the values of J_0 are affected by σ , especially for the observables yielding lower values of J_0 , such as the susceptibility $\chi_c(T)$. On the other hand, the power-law exponent α shows a less pronounced dependence on σ for all datasets. Additionally, the discrepancies between the fit results for different observables can be explained as follows. While $C_p(T)$ and $\chi(T)$ are primarily sensitive to the low-energy part of the distribution, $M(H)$ probes instead the intermediate-to-high energy part most reliably. Indeed, the behavior of $C_p(T)$ at low T (see Fig. 2 (b) of the main text) suggests $\alpha \approx 0.46$, different from the one extracted from $M(H)$. As we use a distribution having same form at low and intermediate energies, one may expect such discrepancies to appear. Additionally, we note that phonons provide an important contribution to $C_p(T)$ and thus the parameters of the random-singlet model also may depend on the modeling of phonon contribution (see below).

Susceptibility and Curie-Weiss law

Here we provide some details regarding the deviation of $\chi^{c,ab}(T)$ from Curie-Weiss behavior. Analyzing our data in the same way as in [25], we found large uncertainties in T_W , e.g. for the interval between 150 K and 300 K we get 23 ± 15 K along the c -axis and -16 ± 7 K for the in-plane (i.e. $a - b$) direction. Expanding the fitting interval to include lower temperatures (while keeping the upper bound of 300 K), we find that the uncertainties diminish, and that the value of T_W for the lower bound under 40 K falls between -3 K and -5 K along the c -axis and between -1 K and -3 K for the in-plane direction. These results suggest weak antiferromagnetic (AFM) correlations.

TABLE S1. The power-law exponents α and the cutoff scale J_0 are obtained by fitting the magnetic susceptibility, magnetization, and heat capacity data with the corresponding confidence intervals with a soft cutoff characterized by the width σ . Fits for χ^{ab} for $\sigma > 10$ K did not converge to a satisfactory accuracy.

Measured Quantity, σ	α ($\sigma = 0$ (K))	α ($\sigma = 5$ (K))	α ($\sigma = 10$ (K))	α ($\sigma = 15$ (K))
$\chi^c(T)$	0.62 ± 0.02	0.60 ± 0.02	0.56 ± 0.02	0.5 ± 0.04
$\chi^{ab}(T)$	0.66 ± 0.01	0.62 ± 0.02	—	—
$M_c(H)$	0.64 ± 0.01	0.62 ± 0.01	0.59 ± 0.02	0.54 ± 0.02
$C_p(T)$	0.55 ± 0.05	0.54 ± 0.06	0.54 ± 0.06	0.54 ± 0.07

Measured Quantity, σ	J_0 (K) ($\sigma = 0$ (K))	J_0 (K) ($\sigma = 5$ (K))	J_0 (K) ($\sigma = 10$ (K))	J_0 (K) ($\sigma = 15$ (K))
$\chi^c(T)$	36 ± 1	34 ± 1	26 ± 2	7 ± 5
$\chi^{ab}(T)$	16.3 ± 0.4	10 ± 1	—	—
$M_c(H)$	67.8 ± 0.4	65.8 ± 0.4	60.5 ± 0.5	52.3 ± 0.5
$C_p(T)$	95 ± 5	95 ± 7	96 ± 7	97 ± 8

TABLE S2. Fitting parameters for the phonon model (S11) with respective confidence intervals. The confidence intervals for a, b, c have been calculated without taking the constraint $a + b + c = 1$ into account.

a	b	c	θ_D (K)	$\hbar\omega_1$ (K)	$\hbar\omega_2$ (K)	$\hbar\omega_3$ (K)
0.36 ± 0.03	$b = 0.13 \pm 0.04$	0.51 ± 0.01	74 ± 15	196 ± 12	97 ± 9	567 ± 13

In Fig. S4 we present $\chi - \chi_0$ multiplied by a function $f(T)$ for fields in the chain (a) and in-plane (b) directions. Colored lines are for $f(T) = 3(T - T_W)$ and black line corresponds to $f(T) = \chi_{RS}(T)/\mu_{eff}^2$. At high temperatures all curves converge to the same value (within error bars). Note that the error bars grow with T as we effectively multiply χ by T at high temperature, and thus the absolute value of the error bar for is enhanced with it. At low temperatures one can see that the colored curves exhibit significant deviations from the high-temperature value. For some values of T_W there is a pronounced dip, while for others it is the marked enhancement towards low T . However, there is no single curve that has neither. In this respect, fits with the RSS model show superior quality (see insets for low temperatures).

Specific heat

Assuming unit cell with six formula units [24], one expects $3 \cdot 126$ phonon branches in $\text{Ba}_5\text{CuIr}_3\text{O}_{12}$. At low temperatures 3 acoustic branches should dominate and we use the Debye model for their contribution

$$C_{Deb}(\theta_D, T) = 9k_B \left(\frac{T}{\theta_D} \right) \int_0^{\theta_D/T} dx \frac{x^4 e^x}{(e^x - 1)^2}. \quad (\text{S9})$$

For higher temperatures the contribution of optical phonons should be included; we use the Einstein model

$$C_{Ein}(\omega, T) = 3k_B \left(\frac{\hbar\omega}{T} \right)^2 \frac{e^{\frac{\hbar\omega}{T}}}{(e^{\frac{\hbar\omega}{T}} - 1)^2}. \quad (\text{S10})$$

We've found that a successful fitting can be performed using Einstein model with three different frequencies. In total, we have used (per formula unit)

$$C_{phon}(T) = C_{Deb}(\theta_D, T)/6 + 125/6(aC_{Ein}^1(\omega_1, T) + bC_{Ein}^2(\omega_2, T) + cC_{Ein}^3(\omega_3, T)), \quad (\text{S11})$$

where $a + b + c = 1$ and $\theta_D, \omega_{1,2,3}$ are fitting parameters. Their values resulting from the fit are $a = 0.36 \pm 0.03$, $b = 0.13 \pm 0.04$, $c = 0.51 \pm 0.01$, $\omega_1 = 196 \pm 12$ K, $\omega_2 = 97 \pm 9$ K, $\omega_3 = 567 \pm 13$ K and the ones for the random singlet part are given in Table S2. The confidence intervals for a, b, c have been calculated without taking the constraint $a + b + c = 1$ into account.

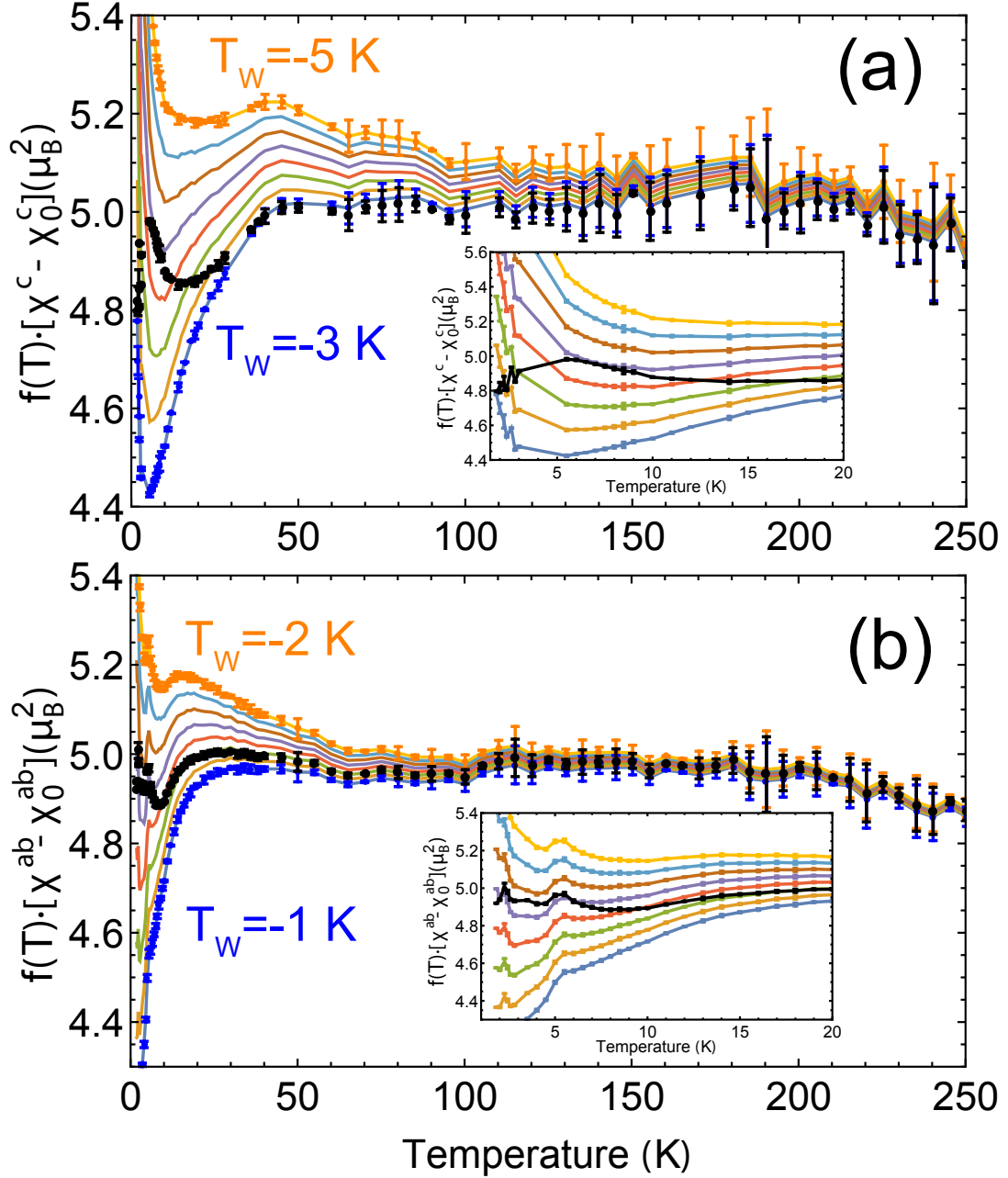


FIG. S4. (a) $\chi^c - \chi_0^c$ multiplied by a function $f(T)$. For colored points $f(T) = 3(T - T_W)$ for several values of T_W between -3 K and -5 K, for $H \parallel c$. Black points: $f(T) = \chi_{RS}(T)/\mu_{eff}^2$. Lines are guide to the eye. At high temperatures all curves converge to μ_{eff}^2 . (b) Same for $\chi^{ab} - \chi_0^{ab}$ and values of T_W between -1 K and -2 K. Kink at around 2 K is due to the equipment noise. The units have been converted from $emu \cdot K/mol$ to μ_B^2 with a prefactor $k_B[erg/K]/N_A/\mu_B^2[erg/G]$.

Magnetization

Obtaining μ_{eff}

To obtain the μ_{eff} value used in the main text, we performed magnetization measurements at 9 T by using a Vibrating Sample Magnetometer (Quantum Design Dynacool) in the temperature interval 2 K to 300 K. The data were taken from the same sample as the one used in high-field studies. In Fig. S5 we present $\chi_{9T} = M(H, T)/H$. For the susceptibility, the curves become linear in T above 50 K, suggesting a Van Vleck term in addition to a

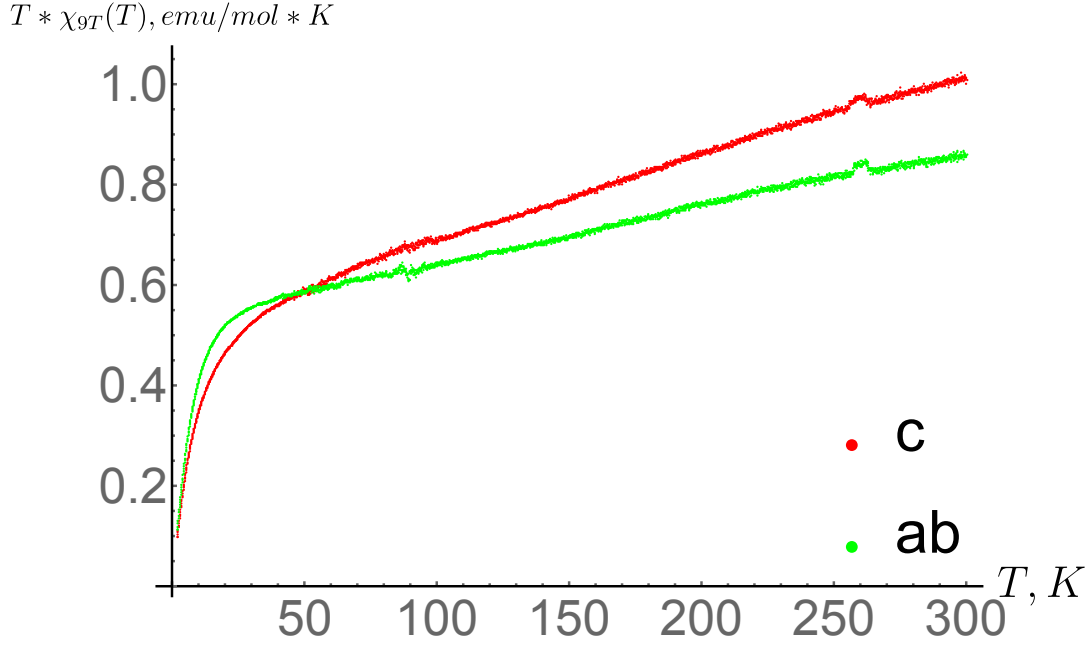


FIG. S5. Susceptibility at 9T field multiplied by the temperature. The weak kink near 260K results from the noise of the equipment.

Curie term. Fitting the curves between 100 and 250 K with $\chi_{9T}^{ab(c)}(T) = \frac{C^{ab(c)}}{T} + \chi_0^{ab(c)}$ we obtain: $C^{ab} = 0.518$ emu/mol*K, $\chi_0^{ab} = 0.0012$ emu/mol; $C^c = 0.513$ emu/mol*K, $\chi_0^c = 0.00174$ emu/mol. From these values one obtains $\mu_{eff}^c = 2.025\mu_B/f.u.$ and $\mu_{eff}^{ab} = 2.035\mu_B/f.u.$. These values are close to the effective moment expected from one Cu^{2+} $\mu_{eff}^{\text{Cu}} = 1.9\mu_B$ and one Ir trimer $\mu_{eff}^{\text{Ir-tr}} = 0.8\mu_B$ [27] moments per formula unit (f.u.): $\sqrt{(\mu_{eff}^{\text{Cu}})^2 + (\mu_{eff}^{\text{Ir-tr}})^2} \approx 2.06\mu_B$.

Note that $\chi - \chi_0$ at the lowest available temperature restricts the possible low-temperature Curie contribution due to unpaired spins to less than 20 % of the high-temperature value. Moreover, the Curie contribution is likely to be much smaller than that, as there are no signs of saturation of $T * \chi$ in Fig. S5 at low temperature.

Calibration of the high-field measurements

The high-field measurements were calibrated with magnetization curves measured at field up to 9 T with SQUID magnetometer (Quantum Design) at 2 K. The value of pulsed-field measurement is taken to coincide with the SQUID measurement at 9 T. The resulting curves are presented in Fig. S6 with 10% error bars for the pulsed-field data, taken for the purpose of illustration, as the sample signal has been rather low.

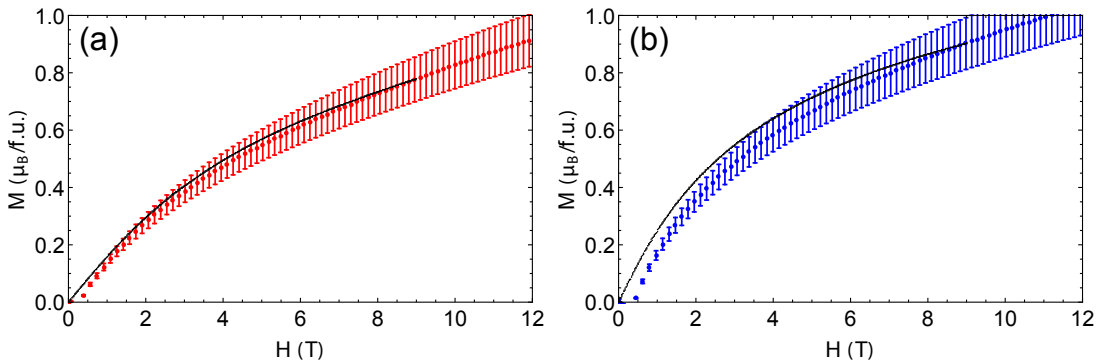


FIG. S6. Pulsed-field magnetization and magnetization measured by SQUID (black) for (a) $H \parallel c$ (b) $H \parallel ab$. 10% error bars are taken the pulsed-field data, as the sample signal has been low.

One can see that the calibration curve does not fit satisfactorily the pulsed-field data for $H \parallel ab$. Furthermore, other issues appear if we proceed with magnetization along ab in high-fields. In Fig. S7 the magnetization is presented after subtracting the Van Vleck contribution assuming it being linear in field (i.e. $M_{VV}(H) = H\chi_0$).

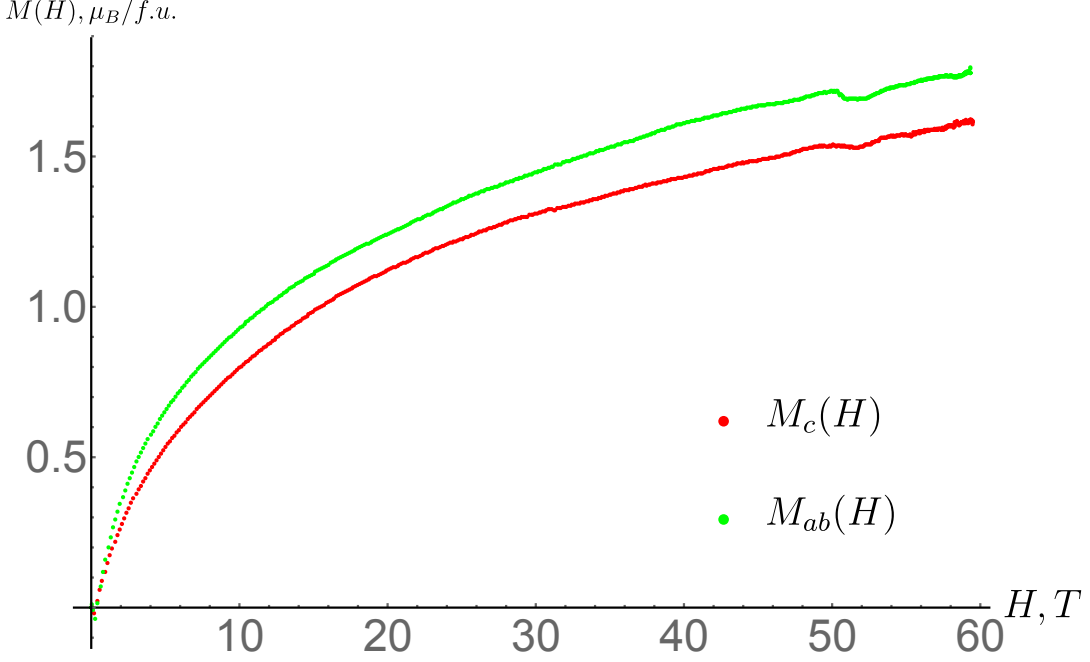


FIG. S7. Magnetization curves at $T = 2$ K after subtraction of the linear Van Vleck contribution.

Because the magnetization does not saturate, the maximal value of the magnetization attained, $M_c^{max} \approx 1.62\mu_B/f.u.$ and $M_{ab}^{max} \approx 1.79\mu_B/f.u.$, should be smaller than the saturation moment μ_{sat} . Assuming that μ_{eff} is realized two $S = 1/2$ spins we have $\mu_{eff} = \sqrt{\mu_{eff,1}^2 + \mu_{eff,2}^2}$, and hence $\mu_{sat} = (\mu_{eff,1} + \mu_{eff,2})\sqrt{\frac{S}{S+1}} = \frac{\mu_{eff,1} + \mu_{eff,2}}{\sqrt{3}} \leq \frac{\sqrt{2}\mu_{eff}}{\sqrt{3}} \approx 1.66\mu_B/f.u.$ This value is smaller than M_{ab}^{max} . If we use the more realistic effective moments for the Cu^{2+} ions ($1.9\mu_b$) and Ir^{4+} trimers ($0.8\mu_b$ [27]), $\mu_{sat} = \frac{2.7}{\sqrt{3}} \approx 1.56\mu_B/f.u.$, which is even smaller than M_c^{max} . Such discrepancy could be attributed to the issues in the pulsed-field measurements for $H \parallel ab$ evident from Fig. S6.

Given the smaller magnitude of the discrepancy for M_c^{max} , we use the $H \parallel c$ data for the analysis in the main text.